Influence of spin on film thickness in elastohydrodynamic starved point contacts

Alberto Porras-Vazquez, Nicolas Fillot, Philippe Vergne, David Philippon, Guillermo Morales-Espejel

Influence of spin on film thickness in elastohydrodynamic starved point contacts

Alberto Porras-Vazquez[1], Nicolas Fillot[1], Philippe Vergne[1], David Philippon[1], Guillermo E. Morales-Espejel[1,2]

[1] Univ Lyon, INSA Lyon, CNRS, LaMCoS UMR5259, F-69621, Villeurbanne, France
[2] SKF Research & Technology Development, Meidoornkade 14, 3992 AE Houten, The Netherlands

Abstract

The roller-end/flange contact in rolling-element bearings represents a crucial design point. Some of the main aspects defining the contact are its particular kinematics, integrating spinning and the occurrence of starved conditions, due to high curvature radii of the region.

In the present study, we present the equations characterizing both spinning and starvation in isothermal EHD contacts lubricated by a Newtonian fluid. After the validation of the model for the case without spin, the analysis focuses, firstly, on characterizing the influence of spinning on the film thickness profile, particularly its global minimum film thickness. Secondly, it aims to evaluate how spinning interacts with starvation in circular contacts, quantifying its effects on the film thickness. Finally, this work provides analytical expressions to predict film thickness in such specific operating conditions.

Keywords: elastohydrodynamic lubrication; spin; starvation; flange roller-end contact.

1. Introduction

The design of high-performant and reliable lubricated mechanical components, such as roller bearings or gear drives, require a deep knowledge of the different phenomena derived from the interaction of their elements and their behavior when exposed to specific operating conditions and fluids. Roller bearings may be subjected to heavy radial loads. However, due to the nature of these, a residual load parallel to the bearing's rotation axis is generally carried by the contact between the roller-end and the ring flange. The understanding of this particular contact is key to control the power losses in the bearing and thus optimize its design. In spite of it, the study of the roller-end/flange contact is not trivial and limited research on this subject is found in the literature as a result of its complexity.

Indeed, the roller-end/flange contact presents an intricate kinematic field when compared to other classic rolling-contact configurations, like ball or roller-on-plane, which have been the focus of extensive studies in the past by authors such as Hamrock and Dowson [1] [2], Chittenden *et al.* [3] [4] or, more recently, Venner and Lubrecht [5]. In addition to the sliding and rolling components identified here, the roller-end/flange contact kinematic field also takes into account a spinning motion, which affects the film thickness generation and thermal effects, amongst other aspects.

The first studies on spinning contacts were not carried out until the early 1970s, when Snidle and Archard [6] and Poon [7] presented some initial and limited conclusions from a theoretical point of view. Thereafter, Dowson *et al.* [8] [9] [10] tackled the behavior of elastohydrodynamic (EHD) isothermal elliptical contacts under various kinematic conditions and analyzed the influence of the kinematic field on the local variations of the film thickness profile. Their conclusions were confirmed years later by the works of Yang and Cui [11] and Zou *et al.* [12]. Moreover, it was observed that spin had little effect on the contact pressure field in either shape or magnitude. Dowson *et al.* pointed out in [10] how the pressure profile is flattened by elastohydrodynamic and piezoviscous effects when high loads were applied. Similar results were noted by Colin *et al.* [13] when the lubricant supply of the contact was limited. Taniguchi *et al.* [14] proposed a predictive formula for the minimum film thickness of spinning contacts based on a reduction factor. Similarly, Zou *et al*. [12] derived analytical expressions for both central and minimum film thicknesses based on numerical data from computational simulations; however, thermal and non-Newtonian effects were omitted from the analysis.

In recent years, a combined effort has been done by Dormois *et al.* [15], Doki-Thonon *et al.* [16] [17] and Wheeler *et al.* [18] [19] to characterize the roller-end/flange contact both numerically and experimentally and delve into the different mechanisms acting on it. Hence, the authors presented a numerical model based on the finite element method [20] and a dedicated test rig for large-size spinning lubricated contacts [21]. Their studies covered the influence of spinning on the friction coefficient, the thermal dissipation and the contact geometry, respectively. However, in all their results, fully flooded conditions were always assumed. This assumption is far from the actual lubrication conditions of the contact. In a complete bearing, lubricant film rupture at each contact outlet determines the lubricant availability of the subsequent contact which, as a result of it, may operate under starved lubrication conditions. Gadallah and Dalmaz [22] proved in fact that starvation constitutes

one of the main factors governing the lubrication of the roller-end/flange contact, being sensitive to the small inlet domain size during pressure build up.

Research on the effects of starvation in EHD contacts can likewise be traced back to the late 1960s and early 1970s. By limiting the lubricant supply, the contact behaves similar to a dry contact. Then, the inlet meniscus, marking the free boundary between the full film and starved domains, approaches the Hertzian contact area. This event bears significant consequences on the film thickness, traction forces, temperature and friction levels, as well as the load-carrying capacity of the contact. The reader may be referred to the works of Wedeven *et al.* [23], Chevalier *et al.* [24], Damiens *et al.* [25] and Svoboda *et al.* [26] for a more in-depth understanding of the phenomenon. Starvation has usually been studied as an isolated event or in conjunction to thermal or geometric effects. However, the authors were not able to find any past or current research combining the topics of starvation and spinning motion. This article aims to expand the literature on this subject and provide a better understanding on the influence of starvation on the film thickness generation of large-size spinning contacts under isothermal and Newtonian conditions. In addition, the study presented herein also seeks to quantify these effects in order to predict the film thickness loss under specific operating and lubrication conditions.

2. Modelling the EHD starved point contact with spin

The model used herein is based on the one previously developed by Doki-Thonon *et al.* [16] [17] and Wheeler *et al.* [18] [19] for evaluating full film EHD contacts, which was in turn inspired by the work of Habchi *et al.* [27] [28]. This model has been quantitatively validated by experiments for a wide range of operating conditions and geometries, with and without spin [17] [18]. In this study, the focus is on the effect of lubricant starvation on film thickness generation in spinning contacts, a configuration not referred in the literature. The numerical model is based on a multiphase approach for which the key parameter is the density of the fluid media all along the contact area and its surroundings (inlet and outlet). The lubricant is considered to be Newtonian, the regime isothermal and the surfaces perfectly smooth. This is justified as a first step in this field, the goal was not to complexify the analysis and to allow the comparison-validation with experiments. Some years ago, Doki-Thonon [16-29] showed that, under fully flooded conditions, the assumptions of Newtonian behavior and, more importantly, of the isothermal regime, led to an overestimation of the film thickness at high load and high spin. However, in presence of lubricant starvation, these operating conditions are experimentally unachievable in a controlled and stable manner, and therefore the validation of any numerical thermal model would have been impossible.

2.1. Spinning kinematics

The relative motion between two contacting bodies results from combining rolling, sliding and spinning. Spinning introduces additional rotational components into the velocity field. In some machine elements, such as rolling element bearings, spinning may be induced by the tilting or skewing of its components. The reader is referred to Figure 1 (left), illustrating a schematic representation of a spinning contact between a spherical-end specimen (solid 2) and a plane (solid 1). Solid 1 and solid 2 rotate with an angular velocity Ω_1 and Ω_2 around an axis marked in red and blue, respectively. The contact area between both solids is colored in yellow.

Figure 1 (right) shows the velocity profile in the contact area, relative to the surface of each solid.

The mean entrainment velocity defined at the center of the contact is expressed as:

$$u_{e,j,0} = \frac{u_{1,j,0} + u_{2,j,0}}{2} \tag{1}$$

with $u_{i,j,0}$ the velocity of solid i in the j-direction, measured at the center of the contact (subscript 0).

With spin, the rolling and sliding conditions vary locally within the contact area. By considering the contact center as the spinning pole, the spinning kinematics can be written as:

$$\begin{cases} u_{i,x}(x,y) = u_{i,x,0} - \Omega_i y \\ u_{i,y}(x,y) = u_{i,y,0} + \Omega_i x \end{cases} \tag{2}$$

with $u_{i,j}$ the velocity of solid i in the j-direction measured at a point (x,y) on the surface of solid i and Ω_i the angular velocity of solid i in the z-direction.

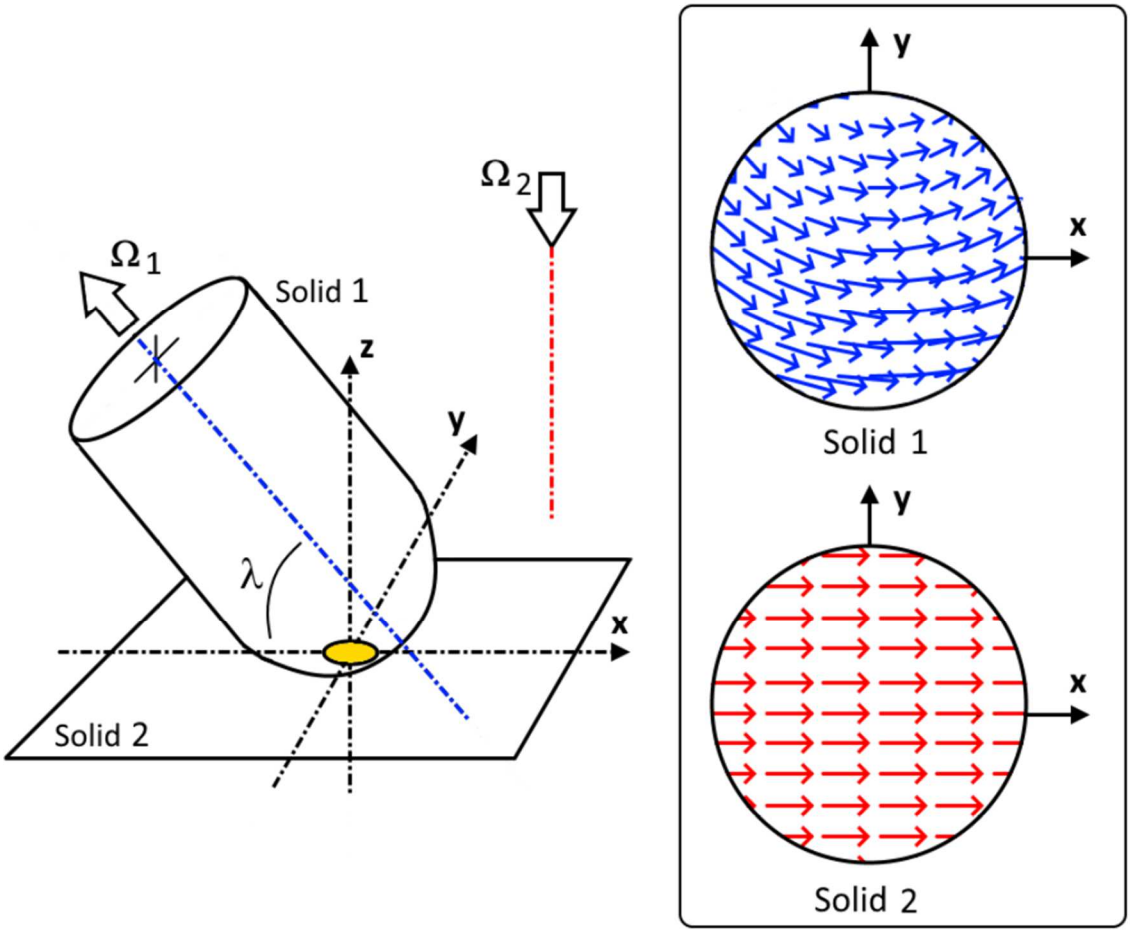

Figure 1. *Left: schematic representation of a spinning contact between a spherical-end specimen (solid 2) and a plane (solid 1). The contact area is marked in yellow. Right: velocity profiles at the contact area on the surface of solids 1 and 2.*

2.2. EHD contact model

The EHD pressure distribution for a point contact can be expressed through the Reynolds equation:

$$\frac{\partial}{\partial x}\left(\frac{\rho h^3}{12\mu}\frac{\partial p}{\partial x}\right)+\frac{\partial}{\partial y}\left(\frac{\rho h^3}{12\mu}\frac{\partial p}{\partial y}\right)-\frac{\partial}{\partial x}\Big((u_{1,x}+u_{2,x})\rho h\Big)-\frac{\partial}{\partial y}\Big((u_{1,y}+u_{2,y})\rho h\Big)=0 \qquad (3)$$

where ρ and μ stands for the density and the viscosity of the fluid and p is the pressure.

The boundary conditions in terms of p are set to ambient pressure along the edges of the computation domain. These are defined at a distance far enough from the contact region so that $\nabla p = 0$. The value of h corresponds to the film thickness and is given by the sum of the gap height between the rigid solids at the contact center h_0, the initial geometry of the surfaces (approximated by a parabolic shape) and the deformation of the solids $\delta(x,y)$. The film thickness equation reads:

$$h(x,y)=h_0+\frac{x^2}{2R_x}+\frac{y^2}{2R_y}+\delta(x,y) \qquad (4)$$

The equivalent body theory [28] is employed to reduce the two solids in contact into a solid with equivalent geometry and physical properties. Thus, R_x and R_y are the reduced curvature radii of the equivalent solid in the x and y-directions, respectively, and E' and ν its Young modulus and Poisson ratio. The deformation $\delta(x,y)$ is calculated using the equivalent solid and the linear elasticity theory. The equivalent solid is clamped at its bottom surface and is hence restricted from any movement.

The load balance equation ensures that the pressure generated by the lubricant film carries the load w applied on the contact. This condition is written as:

$$w=\iint_{S_p} p(x,y)\,dx\,dy \qquad (5)$$

with S_P the pressurized contact area.

The characterization of the lubricant viscosity μ through a high-pressure viscometer, allows to model its dependency with pressure and temperature by a modified Yasutomi-WLF correlation [30]:

$$\mu(p)=\mu_g\times 10^{\frac{-C_1\left(T_0-T_g(p)\right)F(p)}{C_2+\left(T_0-T_g(p)\right)F(p)}} \qquad (6)$$

where $T_g(p) = T_{g,0} + A_1 \ln(1 + A_2 p)$ and $F(p) = (1 + b_1 p)^{b_2}$. μ_g is the viscosity at the glass transition, $T_{g,0}$ is the glass transition temperature at ambient pressure and A_1, A_2, b_1, b_2, C_1 and C_2 six constants dependent on the fluid.

The pressure dependency of the density ρ is described by the Murnaghan equation of state:

$$\frac{\rho_0}{\rho} = \left(1 + \frac{K_0'}{K_0} p\right)^{-\frac{1}{K_0'}} \tag{7}$$

where ρ_0 and K_0 are the density and the bulk modulus measured at ambient pressure and temperature T_0.

The bulk modulus K_0 can in turn be written as:

$$K_0 = K_{00} e^{-\beta_k T_0} \tag{8}$$

with K_{00} the value of K_0 when T = 0 K and β_k the bulk modulus-temperature coefficient.

A validation of the initial numerical model presented here is provided by Doki-Thonon *et al.* in [17], where the film thickness profiles of two distinctly spinning contacts were compared to the experimental profiles obtained from a specialized test rig under identical operating conditions.

2.3. Starvation

The approach commonly employed to tackle starved EHD contacts is the Elrod-Adams algorithm [31] [32]. This method introduces a variable θ into the classical Reynolds equation to attenuate the effects of the Couette flow in thin films. A unique solution of the now modified Reynolds equation is found by applying the complementary condition:

$$p(x, y) \cdot \big(1 - \theta(x, y)\big) = 0 \tag{9}$$

where $p(x, y) > 0$ and $\theta = 1$ in the full film region and $p(x, y) = 0$ and $\theta \leq 1$ in the incomplete film.

At the same time, the variable θ is defined as a function of the local film thickness of the fluid h_f:

$$\theta(x, y) = \frac{h_f(x, y)}{h(x, y)} \tag{10}$$

Although this approach is extensively used in the field with success, the inclusion of an artificial parameter θ makes the overall method lack the physical foundation of the Navier-Stokes equations.

Additional issues related to the performance and quality of the method have been highlighted throughout the work of Bayada *et al.* [33] [34]. These issues concern mainly conditions at the free boundary and the contact region. Despite the compliance of the set of equations with mass conservation, it has been noticed that the variations of θ and the pressure gradient are discontinuous at the film formation boundary. Gu *et al.* [35] proposed a transition region to smooth the jump in both functions, but the aforementioned conditions would no longer apply. As stated for Equation (9), multiple pressure values are associated to a unique θ in the full film contact region, which evidences that the resolution of the equations is not trivial.

At the film rupture boundary, cavitation takes place in the form of subambient pressure values. Typically, cavitation is omitted from the evaluation of EHD contacts, as the pressures found at the contact outlet are several orders or magnitude smaller than the in-contact pressure values, and thus renders variations in the contact film thickness profile negligible. These subambient pressures are computationally corrected by means of the Reynolds (also known as Swift-Stieber [36] [37]) boundary condition and are set to zero, alongside the pressure gradient in the same region. Similarly, Wu [38] introduced a penalty term in the original Reynolds equation, which deemed similar results and agreed with mass conservation. Experimentally, these cavitated pressure values have been observed and measured by different authors [39] [40] [41]. Dowson and Taylor [39] argued that the conditions found at the contact outlet could in fact have an effect on the degree of starvation upstream of the contact inlet, as it reduced the lubricant replenishment flow carried by the surface of the rolling element. The original Elrod-Adams algorithm considered cavitation through a θ-dependent binary switch function, which made the starved problem highly nonlinear due to the hyperbolic and elliptical nature of the functions. Hence, to improve the convergence and the stability of the solution, Vijayaraghavan and Keith [42] coupled the bulk modulus of the fluid to the switch function and the θ variable, and Fensanghary and Khonsari [43] suggested a continuous switch function instead of the binary one.

More recent efforts focus on defining the lubricant as a homogeneous biphasic fluid with compressible character. One can highlight the models from Elrod [32], Shalin *et al.* [44], van Odyck and Venner [45], and Bayada and Chupin [46], which were thoroughly compared in [46]. These models are built on an isentropic assumption of the fluid to describe the evolution of the lubricant density (and occasionally also its viscosity) with pressure along three distinct phases. The lubricant can thus be found in a pure liquid or vapor phase, as well as a mixture phase containing variable fractions of the aforementioned states with pressure. The transition between each phase takes place at specific pressure values. The procedure to evaluate these transition pressures changes for each model employed.

Most of the starved models used, including the Elrod-Adams algorithm, consider relative pressure values. The Elrod-Adams algorithm omits the mixture phase and considers an immediate transition between the pure liquid and vapor phases (reflecting the pressure and cavitated regions, respectively) according to a step-like function at the ambient pressure, $\mathrm{p} = 0$ in relative terms. In turn, Bayada and Chupin [46] and Bayada [47] establish the value of the wet point pressure $\mathrm{P_{vm}}$ and bubble point pressure $\mathrm{P_{sat}}$ as the specific conditions marking the transition between the vapor and mixture phases and the mixture and liquid phases of the lubricant, respectively. The calculation of these two pressure values is expressed exclusively in terms of the properties of the lubricant in its vapor and liquid phases:

$$P_{vm} = \rho_v c_v^2 \tag{11.a}$$

$$P_{sat} = \rho_v c_v^2 - N \log\left(\frac{\rho_v^2 c_v^2}{\rho_l^2 c_l^2}\right) \tag{11.b}$$

with:

$$N = \frac{\rho_v c_v^2 \rho_l c_l^2 (\rho_v - \rho_l)}{\rho_v^2 c_v^2 - \rho_l^2 c_l^2} \tag{12}$$

where ρ_v and ρ_l are the density of the vapor and liquid phases, and c_v and c_l are the speed of sound of the vapor and liquid phases, respectively.

In the present study, the density of the gap between the mating surfaces is described in terms of an equivalent and uniform fluid containing variable fractions of air and lubricant. The behavior of the equivalent fluid is bounded by the pressures $P_{g,sat}$ and $P_{g,vm}$, with subscript g referring to the gap.

- Above the bubble point pressure, the fluid behaves as a pure liquid, that is, the gap contains only liquid lubricant and no air. This condition delimits the contact region. Therefore, the properties of the gap evolve according to the rheological law of the lubricant.

$$\rho_g(p) = \rho_f(p) \quad \text{if } p \geq P_{g,sat} \tag{13a}$$

- Below the wet point pressure, the gap contains air and lubricant in vapor phase. This corresponds to the cavitated region at the contact outlet. Similar to other biphasic fluid models [44] [45] [46], the density of the equivalent fluid is assumed to remain constant with pressure.

$$\rho_g(p) = \rho_{g,v} \quad \text{if } p \leq P_{g,vm} \tag{13b}$$

- The mixture phase is associated to the conditions found upstream of the contact inlet. Here, the evolution of the density becomes independent of pressure, as the proportion of air varies with the geometry of the gap. This can be seen for points distant from the contact region: multiple gap density values are identified to the ambient pressure conditions.

$$\rho_g(p) = \rho_f(p)\frac{h_{oil}}{h(x,y)} + \rho_{g,v}\left(1 - \frac{h_{oil}}{h(x,y)}\right) \quad \text{if } P_{g,vm} < p < P_{g,sat} \tag{13c}$$

ρ_f is the density of the fluid following the before stated rheological law. The value of h_{oil} is specified at the edge of the computational domain. The proportion between the volumes of air and lubricant at the boundary defines the specific values of $P_{g,vm}$ and $P_{g,sat}$, through the evaluation of the equivalent fluid's properties $\rho_{g,v}$ and $c_{g,v}$. These parameters are in turn dependent on the individual properties of the air and the lubricant and their ratio. Given that the density and the speed of sound in the oil medium are lower than in the air, an increase of

the degree of starvation results in a more important bubble point pressure. Therefore, the inlet meniscus tends to occur closer to the Hertzian contact area.

3. Numerical model validation

The numerical model has been validated experimentally by means of a classical ball-on-disc tribometer, for both fully flooded and starved conditions and in the absence of spin. A complete description of the test rig can be found in [48] [49]. The contact is made between a steel ball with a curvature radius $R_x = R_y =$ 12.7 mm and a glass disk coated with a semireflective chromium layer. White light interferometry [50] [51] was used for evaluating the film thickness in the contact area. For measuring thin films (below 100 nm), a glass disk with an additional silica spacer layer was used instead. The ball and the disk are driven independently by two brushless motors. An amount of lubricant enough to fully flood the test ball was initially smeared on the surface of the disk.

In order to account for the starved lubrication conditions, the test rig has been modified following the experimental work from Svoboda *et al.* [26]. A steel roller $(D = R_x/R_y = 0.123)$ was placed upstream of the test ball to control the height of a uniform lubricant layer supplied to the contact. A wiper was used to manually scrape off lubricant from the surface of the disk, in front of the roller. The roller is mounted on a carrier at the end of a lever and is supported by four small bearings. It can be charged to a load of 30 N by compressing a spring at the opposite side of the lever where the carrier is found. A load sensor attached underneath of the lever registers the load value. On the other hand, the roller is directly entrained by the rotation of the disk, assuming nominal pure rolling conditions. The conditions are considered to be those of smooth and isothermal contacts due to the very low surface roughness and the applied lubricant and contact parameters.

The roller is useful for determining the film thickness of the lubricant layer h_{oil} feeding the test ball. Consider the diagram in Figure 2, representing a side view of the two rolling elements and the disk. h_{ci} is the central film thickness of contact i (i = 1 for the roller-disk contact and i = 2 for the ball-disc contact). δ_{1i} is the film thickness exiting contact i that is carried by the disk, while δ_{2i} is the film thickness carried by the rolling element back to the inlet of contact i. h_s is the total film thickness at the outlet of the roller-disk contact ($h_s = \delta_{11} + \delta_{21}$).

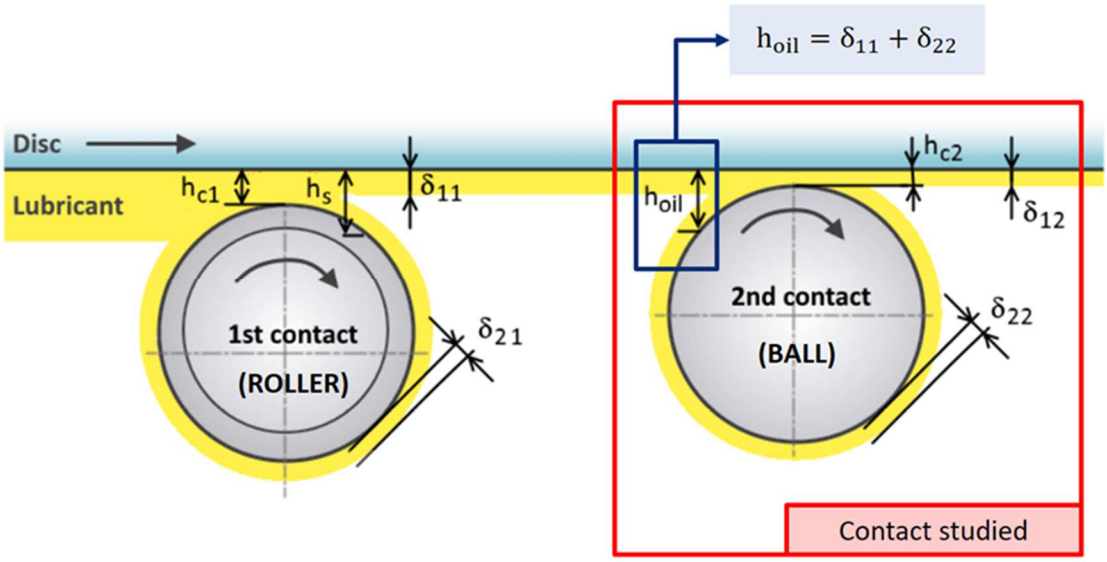

Figure 2. *Side view representation of the roller-ball-disk system, inspired from [26].*

Under pure rolling conditions between all rolling elements, one can write:

$$h_{oil} = 0.5 \cdot \left(h_{c1} \cdot \frac{\rho_{c1}}{\rho_0} + h_{c2} \cdot \frac{\rho_{c2}}{\rho_0} \right) \tag{14}$$

with ρ_c the density of the lubricant at the center of the contact and ρ_0 the density at ambient conditions.

A synthetic polyol ester-based oil (henceforth, lubricant 1) was selected for the validation tests. The coefficients corresponding to the modified Yasutomi-WLF correlation are reported in the Annex in Table 5, while the coefficients of the Murnaghan EOS are given in Table 6.

The entrainment velocity of the rolling elements was set to 0.16 m/s, the load for both roller and ball to 30 N and no spinning motion was introduced. The oil supply was varied to achieve multiple degrees of starvation: from a flooded contact (h_{oil} = 281.5 nm) down to a severely starved one (h_{oil} = 34.6 nm). The operating conditions of the test ball and the roller are summarized in Table 1.

Parameter [Unit]	Test ball	Roller
u_e [m/s]	0.16	0.16
w [N]	30	30
R_x [mm]	12.7	10
R_y [mm]	12.7	81.4
p_H [GPa]	0.52	0.34
T [°C]	25	25
μ_0 [mPas]	148.0	148.0
α^* [GPa^{-1}]	21.2	21.2

Table 1. *Operating conditions of the test ball and the roller.*

A selection of film thickness measurements is gathered in Table 2. The experimental central and minimum film thickness (noted $h_{c,exp}$ and $h_{m,exp}$, respectively) are compared to the corresponding values from the present numerical model (h_c and h_m) as well as the prediction made by Chevalier *et al.* [24] ($h_{c,Chev}$ and $h_{m,Chev}$), all being presented in their dimensionless form.

h_{oil} [nm]	$h_{c,exp}$ [nm]	$h_{m,exp}$ [nm]	$h_{c,Chev}$ [nm]	$h_{m,Chev}$ [nm]	h_c [nm]	h_m [nm]
281.5	246.8	106.1	212.2	108.3	283.6	153.7
240.3	179.7	94.0	171.0	87.4	171.0	112.6
132.1	110.4	77.9	110.4	67.1	110.4	82.3
34.6	30.3	28.1	30.3	26.0	34.6	32.5

Table 2. *Experimental central and minimum film thickness in the ball-disc contact compared to the predictions from Chevalier et al. [24] and results from the present numerical model.*

The numerical film thickness map for the starved case h_{oil} = 240.3 nm from Table 2 has been plotted at the left side of Figure 3 using the color scale from the experimental calibration curve. The experimental interferogram obtained under identical operating conditions is shown at the right side of Figure 3. The representative film thickness values for the two pictures are reported in Table 2.

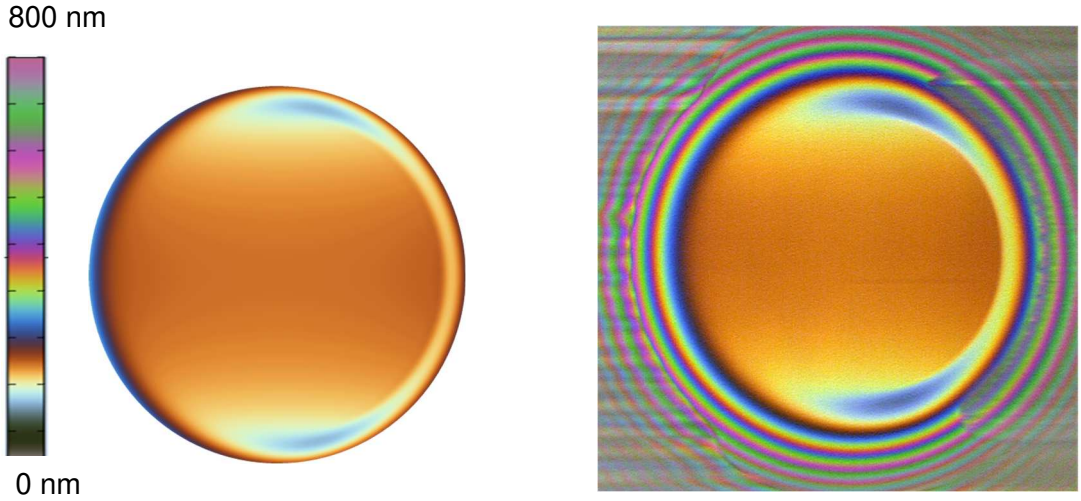

Figure 3. *Numerical solution (left) and experimental interferogram (right) obtained for the oil supply h_{oil} = 240.3 nm (see Table 2), represented with the same color scheme. The main direction of the flow is from left to right.*

The comparison of the experimental and calculated film thickness values in Table 2 and the film thickness distributions in Figure 3 show a good agreement between the approaches. The relative error on the h_c starved measurements is found to be below 5%. On the other hand, it is revealed that the computational model slightly overestimates the value of h_m at the side lobes, in particular, in the case of the more flooded contacts. The numerical results also

reflect the asymptotic behavior described by the Chevalier model [24] in that the central film thickness does not surpass the film thickness of the lubricant supply h_{oil}.

4. Results and discussion

The following sections present a series of numerical results from a steel-on-steel (E = 210 GPa and ν = 0.30) contact between a spherical-end specimen and a plane. A low viscosity mineral base oil (henceforth, lubricant 2) was chosen for this study (μ_0 = 11.4 mPas and α^* = 2.21 x 10^{-8} Pa^{-1}). The different parameters for the rheological characterization of the lubricant are listed in Tables 5 and 6 in the Annex. The temperature was set to 30 °C. Isothermal, Newtonian and stationary conditions are applied.

In order to introduce the notations assumed in the next sections for the representative film thickness values, Figure 4 presents the interferogram of a spinning contact. The dashed black line represents the inlet streamline with entrainment speed u_e, h_{max} is the maximum film thickness in the contact area, h_c the film thickness at the geometrical center of the contact and h_m the minimum film thickness, with subscripts + and - indicating the side of the contact.

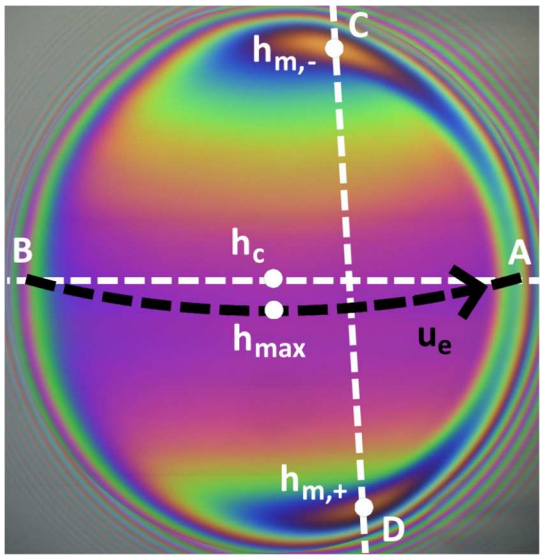

Figure 4. *Interferogram [29] of a spinning contact with the representative film thickness points marked. The center of rotation of the ball is located above the figure.*

4.1. Influence of spin in fully flooded lubrication

The results showcased in this section concern flooded lubrication conditions. In order to evaluate the effect of spin on the film thickness, a wide range of contact cases was studied. The curvature radius R_x was kept constant at a value of 80 mm. The entrainment velocity was changed between 0.5 and 10 m/s, while the normal load was varied between 120 and 2675 N. The spin rotation velocity of the solid was also changed between 0 and 5000 rad/s.

The particular operating and contact conditions applied in this section are summarized in Table 3.

Parameter [Unit]	Value
u_e [m/s]	0.5 - 10
w [N]	120 - 2675
Ω [rad/s]	0 - 5000
R_x [mm]	80
R_y [mm]	80
T [°C]	30
μ_0 [mPas]	11.4
α^* [GPa^{-1}]	22.1

Table 3. *Operating conditions of the contact.*

The set of operating conditions chosen was transcribed into a set of Moes dimensionless parameters [52], given by the expressions:

$$L = (\alpha^* E') \left(2 \frac{\mu_0 u_e}{E' R_x} \right)^{0.25} \tag{15.a}$$

$$M = \left(\frac{w}{E' R_x^2} \right) \left(2 \frac{\mu_0 u_e}{E' R_x} \right)^{-0.75} \tag{15.b}$$

Thus, the aforementioned operating conditions lead to a calculation domain comprised between $L \in [4.7, 9.9]$ and $M \in [40.8, 851]$, covering a significant portion of the full EHL range.

Figures 5 and 6 present the variation of the representative film thicknesses with respect to L and M, respectively, for the spin domain specified above. In Figure 5, the value of M was kept constant at 272 and in Figure 6 L = 6.6. The results are expressed as a ratio $h/(h)_{ff,ns}$, where $(h)_{ff,ns}$ is the film thickness value at the same point under fully flooded conditions (subscript ff) and no spin (subscript ns).

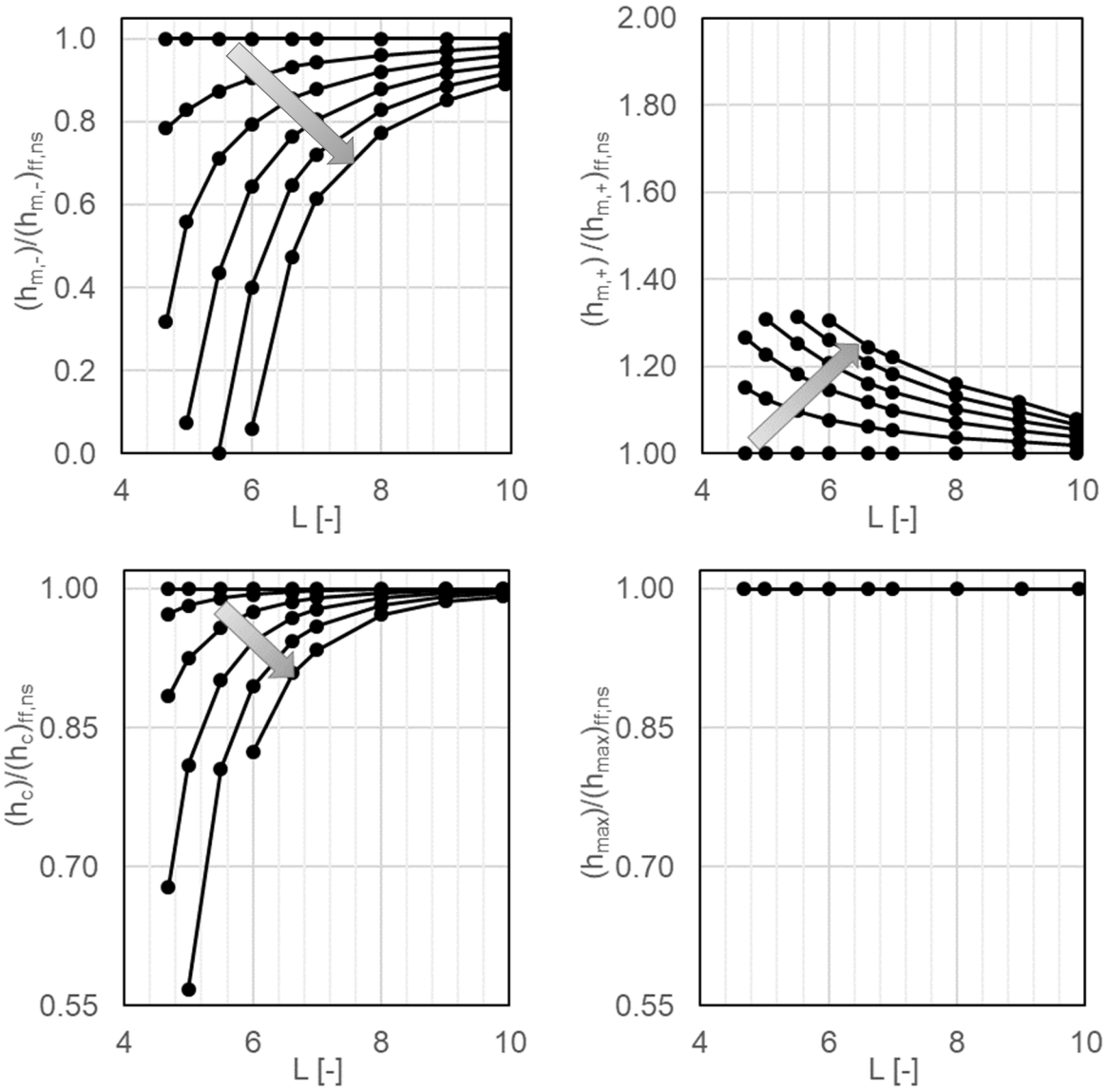

Figure 5. *Variation of the relative representative film thicknesses with the dimensionless parameter L for various spin cases (M = 272). The arrow indicates the direction of increasing spin value (from 0 to 5000 rad/s, in steps by 1000 rad/s).*

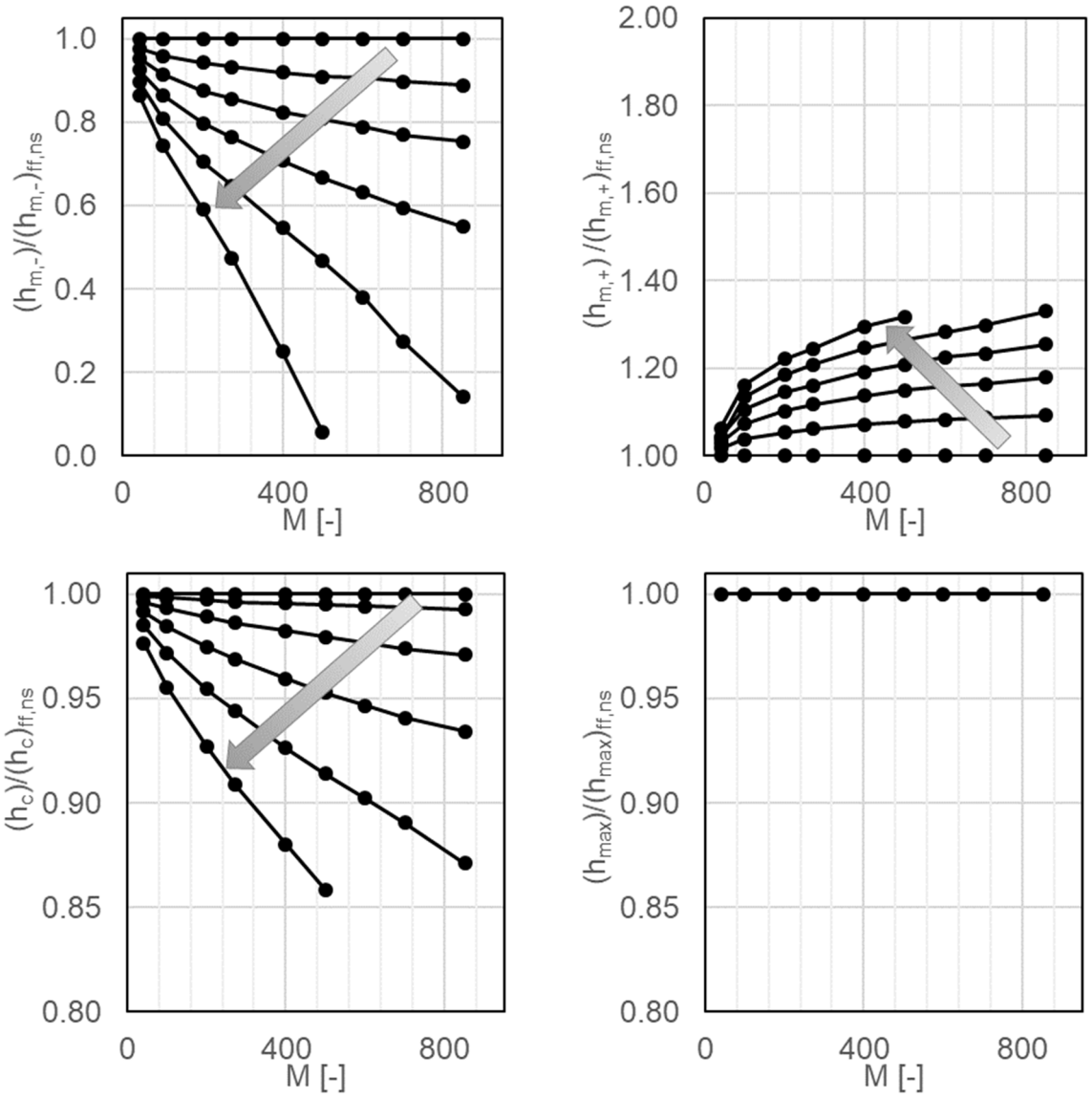

Figure 6. *Variation of the relative representative film thicknesses with the dimensionless parameter M for various spin cases (L = 6.6). The arrow indicates the direction of increasing spin value (from 0 to 5000 rad/s, in steps by 1000 rad/s).*

In general, the opposite trends followed by $h_{m,+}$ and $h_{m,-}$ reveal an increasing dissymmetry in the contact region due to spin. This variation is not uniform: the film thickness reduction on one side lobe ($h_{m,-}$) occurs at a much faster pace than the increase in its other lobe ($h_{m,+}$). At the same time, the effect of the dissymmetry is also shown in the film thickness at the center region of the contact. While the value of h_c decreases, the maximum film thickness stays closely the same regardless of the spin value. In reality, the film thickness value at the geometrical center of the contact ($h_c = h_{max}$ under no spin condition) is displaced with spin from the contact center, in the direction of increasing local speed.

The computed film thickness ratios tend to unity for high L and low M values and, conversely, tend to vary with low L and high M; the value of spin further enhances this last effect. In fact,

the effects of spin are the most noticeable when the pressure distribution becomes more Hertzian-like and when the oil layer becomes thinner and thinner, i.e. when lower speeds and high normal loads are in place. As it can be anticipated from Equation (15), similar results could also be expected for low curvature radii (a smaller contact area leads to a higher influence of the load) and low lubricant viscosities (high mobility of the lubricant). Finally, when changing the value of the curvature radius (keeping R_x equal to R_y), it was observed that identical (L, M) pairs lead to comparable results as those of Figures 5 and 6, meaning that the curves still apply for different solid geometries.

The value of $h_{m,-}$ is critical for the correct operation of rotating elements. Indeed, under specific speed, load and spin conditions, the amount of oil in this region might not be enough and the contact might so become more prone to damage or failure. Special attention should thus be put into predicting the value of this critical film thickness with a fair degree of accuracy. Taniguchi *et al.* [14] quantified the variation of $h_{m,-}$ in terms of a dimensionless spin-to-roll ratio, which is in turn defined as a function of the spin rotational velocity Ω, the entrainment speed u_e and the curvature radius R_x. The domain of the study conducted by Taniguchi *et al.* [14] was limited to spin-to-roll ratios between 0 and 25. They determined different linear trends whose slopes were assumed to depend solely on the load, neglecting other operating or geometric parameters. However, plotting the set of points in Figures 5 and 6 following the same guidelines reveals that these trends tend to lose their linearity and curve at high spin-to-roll ratios.

The present authors propose an alternate definition of this ratio and use the contact radius a instead of R_x to account for the effects of the normal load on the contact area. The new definition for the spin-to-roll ratio then reads:

$$B = \frac{2\Omega a}{u_e} \tag{15}$$

Figure 7 presents the plot of the points introduced in Figures 5 (in blue) and 6 (in yellow) for various L and M pairs following the above criteria. The film thickness reduction is expressed as $C_{sp} = 1 - (h_{m,-})_{ff,sp}/(h_{m,-})_{ff,ns}$, with $(h_{m,-})_{ff,sp}$ the critical minimum film thickness under fully flooded (subscript ff) and spinning (subscript sp) conditions and $(h_{m,-})_{ff,ns}$ the value at the same point under fully flooded conditions and no spin (subscript ns). By using the new definition of the spin-to-roll ratio B, it can been seen that all the previous points tend to collapse into a unique curve, regardless of their operating conditions. The best fit obtained by least-squares regression gives the following expression:

$$C_{sp} = 0.26\left(e^{0.27B} - e^{-0.1B}\right) \tag{16}$$

The data has been completed with experimental measurements extracted from the work of Doki-Thonon [29]. In this case, the contacts were performed between a steel spherical-end specimen (R_x = 80 mm) and a glass disk. The entrainment velocity was varied between 1 and 2 m/s, the load between 400 and 800 N, and the spin rotational velocity between 716 and 1050 rad/s. The lubricant employed was lubricant 2. The temperature was set to 30°C.

The predicted behavior is traced with a continuous line. Two arrows indicate the direction of increasing spin values and $h_{m,-}$ reduction.

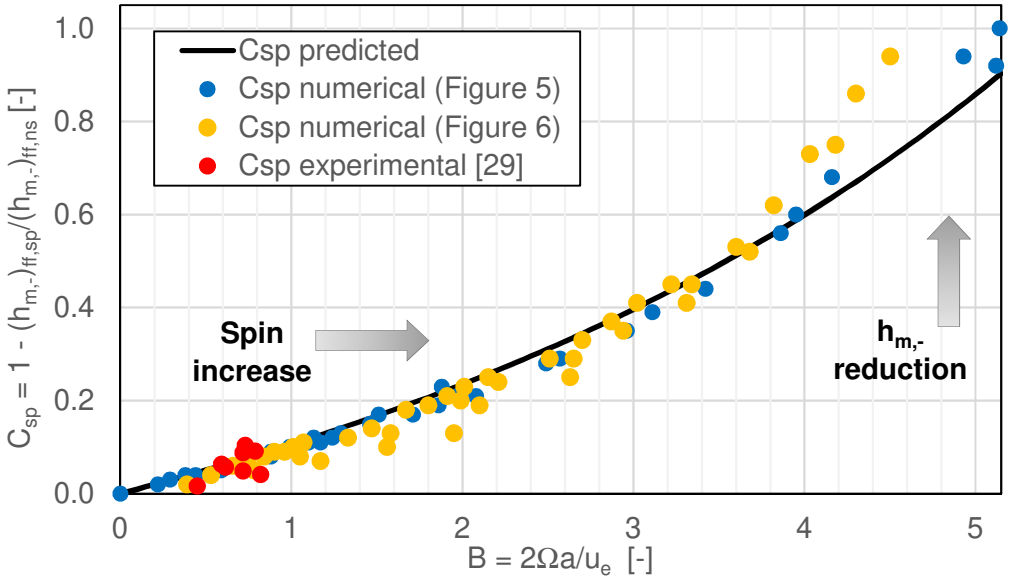

Figure 7. *Effect of the spin-to-roll ratio B upon the critical minimum film thickness for different operating conditions. Experimental points calculated from data extracted from [29].*

The graph shows a continuous decrease of the critical minimum film thickness with spin, regardless of the operating conditions and geometric parameters chosen. The maximum deviation with respect to the predicted behavior corresponds to cases with high B ratios, due to either high spin velocities or C_{sp} rates close to a unitary value, when the contact presents a very thin film at its critical side. The experimental C_{sp} points adjust well to the predictive curve. They concern spinning point contacts subjected to $L \in [5.6, 6.6]$ and $M \in [135, 460]$; R_x = 80mm and the lubricant employed was lubricant 2. The film thickness reduction values presented by Taniguchi *et al.* [14] cannot be compared to the prediction behavior, as they studied elliptical contacts and the present study only concerns circular contacts.

Taking into account the above behavior, an initial expression for estimating the critical minimum film thickness of circular contacts under fully flooded and spinning conditions $(h_{m,-})_{ff,sp}$ is written:

$$(h_{m,-})_{ff,sp} = (h_{m,-})_{ff,ns} \cdot (1 - C_{sp}) \qquad (17)$$

with C_{sp} the film thickness reduction factor due to spin, described in Equation (16), and $(h_{m,-})_{ff,ns}$ the critical minimum film thickness under fully flooded conditions and no spin.

4.2. Influence of spin in starved lubrication

The results presented in this section explore the influence of spin on starved circular contacts. A series of simulations combining variable amounts of spin and starvation degrees was performed. The curvature radius R_x was set to 80 mm. The system was loaded with 800 N and an entrainment speed of 2 m/s was applied. The spin was varied through the angular velocity of the upper solid Ω, resulting in spin-to-roll ratios between 0 (no spin) and 3.7 (high spin). The operating and contact conditions applied in this section are summarized in Table 4.

Parameter [Unit]	Value
R_x [mm]	80
R_y [mm]	80
u_e [m/s]	2
Ω [rad/s]	0 - 5000
B	0 - 3.7
w [N]	800
P_H [GPa]	0.71
r_c [-]	0 - 192
T [°C]	30
μ_0 [mPas]	11.4
α^* [GPa^{-1}]	22.1

Table 4. *Operating conditions of the contact.*

The results are displayed in Figure 8. The curves represent the variations of the local maximum (h_{max}) and critical minimum ($h_{m,-}$) film thicknesses with the amount of lubricant found upstream of the contact inlet (h_{oil}). The data are shown in dimensionless form $R = h/h_{c,ff}$, where $h_{c,ff}$ is the film thickness at the geometrical center under fully flooded conditions and no spin. The dimensionless form of the lubricant supply (r_c) also takes into account the compressibility effect of the lubricant, such that $r_c = h_{oil}/(h_{c,ff} \cdot \overline{\rho_c})$, where $\overline{\rho_c} = \rho/\rho_0$ is the dimensionless density. The R value predictions of the Chevalier model [24] are plotted in a continuous line and concern the no-spin results only. Additionally, the two characteristic asymptotes from the analytical model have been traced in dashed lines. The asymptote $R_c = 1$ when $r_c \geq 1$ represents the limit imposed by the fully flooded contact and considers that the remaining oil flows around it. The asymptote $R_c = r_c$ when $r_c \leq 1$ limits the oil supply of the contact to the total amount of oil on the track. Separate grey arrows indicate the direction of an increasing spin or degree of starvation.

The comparison between the Chevalier and computational models reveal an average relative deviation of 9.8% on h_c and 9.5% on h_m, for the specific operating conditions defined here and no spin.

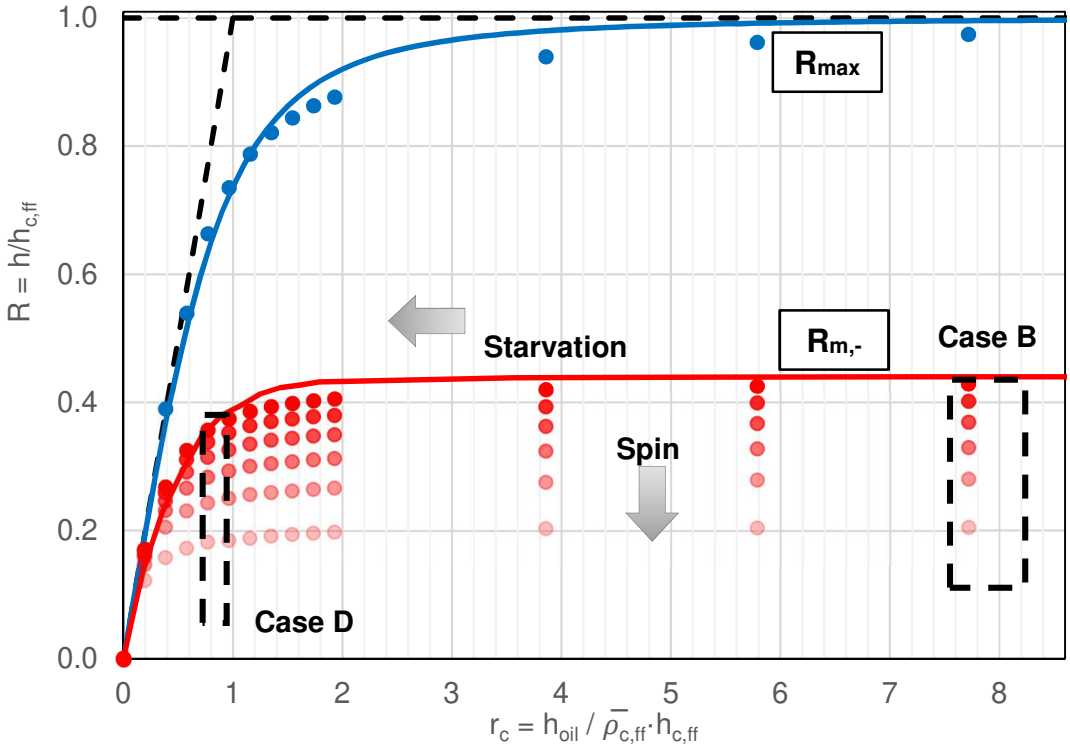

Figure 8. *Dimensionless maximum (R_{max}, in blue) and critical minimum ($R_{m,-}$, in red) film thickness variations with respect to the dimensionless oil supply (r_c) for different spin velocities given by $\Omega = 0 - 5000\ rad/s$ in steps of 1000 rad/s (u_e = 2 m/s, w = 800 N, T = 30°C, R_x = 80 mm). The predictions of the Chevalier model [24] are plotted in continuous lines and concern the no-spin results only.*

The data plotted in Figure 8 shows the decrease of the local maximum and critical minimum film thickness with starvation following the two asymptotic trends described above. A critical oil supply value delimiting the behavior between the fully flooded and starved domains can be estimated at $\mathrm{r_c} \approx 5$. This value supposes a reduction of 5% on $\mathrm{h_c}$ with respect to its fully flooded value. When introducing a spinning motion, the maximum film thickness does not vary, as noticed in Section 4.1. However, the critical minimum $\mathrm{h_{m,-}}$ is reduced. In this case, the asymptotic behavior of the curves is kept, but the transition between the fully flooded and starved domains moves closer towards weaker $\mathrm{r_c}$ values. To account for the particular and combined effects of spin and starvation, four specific cases have been extracted from Figure 8, two of which (identified as Case B and Case D) were highlighted in the same figure. The corresponding dimensionless film thickness profiles of the contacts in the transverse direction of the flow are illustrated in Figure 9. They are represented in terms of $\mathrm{R = h/h_{c,ff}}$ to better quantify the variations in film thickness with respect to its fully flooded and no-spin case. An arrow indicates the direction of an increasing spin or degree of starvation.

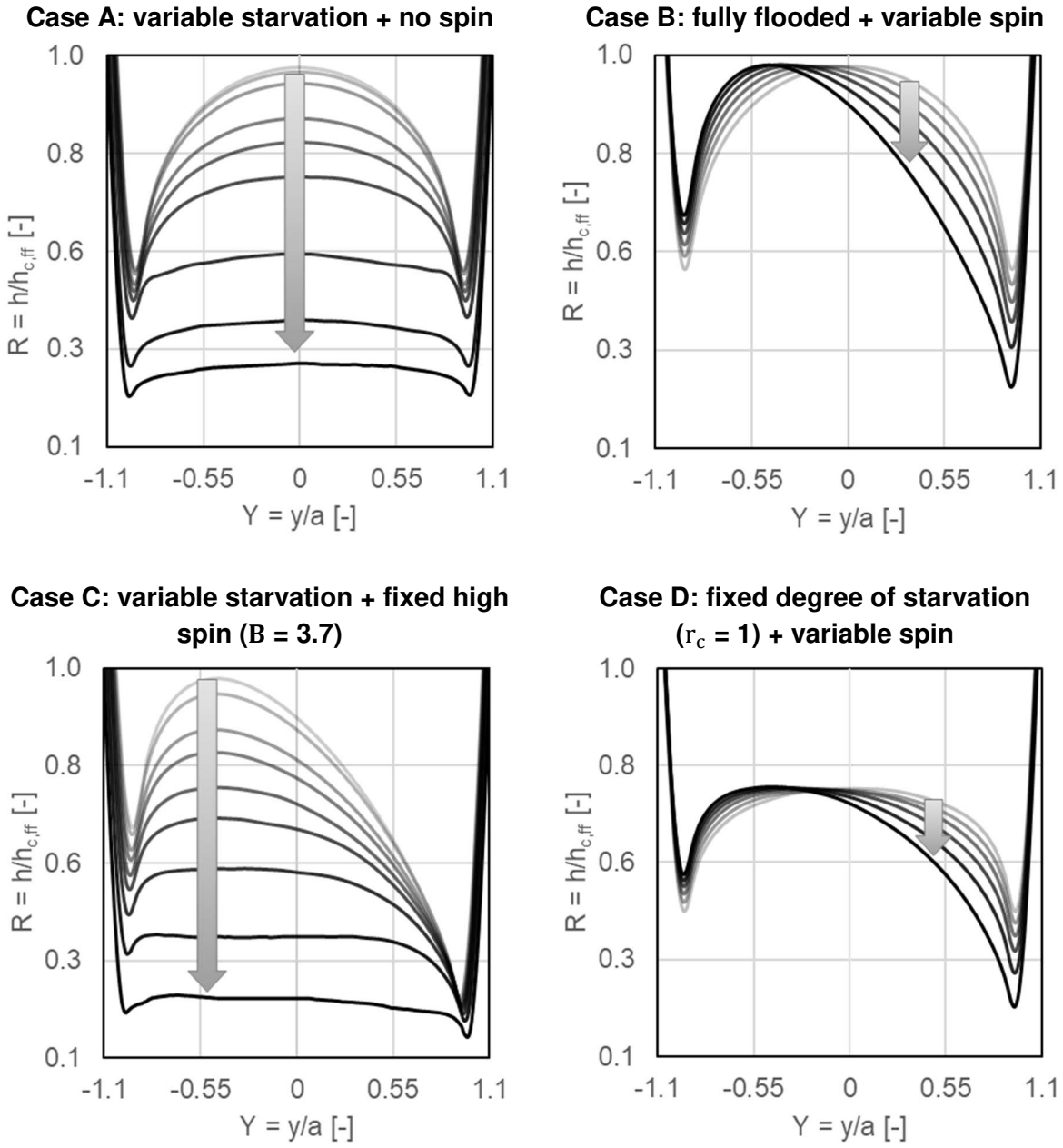

Figure 9. *Transversal film thickness profiles for different scenarios extracted from Figure 8. The arrows indicate the direction of increasing spin (Cases B and D) or degree of starvation (Cases A and C).*

Case A corresponds to contacts with no spin ($\Omega = 0$ rad/s) and variable degrees of starvation. The film thickness profiles reveal a symmetric contact with respect to the direction of flow whose overall film thickness is reduced with the amount of lubricant available. This reduction happens at a faster pace in the center than in the rest of the contact area (75% total reduction of h_c against 40% for h_m with regards to the cases displayed).

Case B in Figure 9 corresponds to fully flooded contacts with variable amounts of spin (from 0 to 5000 rad/s, in steps of 1000 rad/s), as shown in Figure 8. The previously displayed

symmetry of the contact is now lost due to variations in the velocity field. Indeed, the local minima (now distinguished between $h_{m,+}$ for $Y < 0$ and $h_{m,-}$ for $Y > 0$) differ in the film thickness profiles. In the $Y > 0$ area, where a slower velocity occurs, a thinner h_m value than in its counterpart in the $Y < 0$ region is computed. In addition, the effect of spin has a greater impact in the low velocity region (35% total film thickness reduction against 15% film thickness increase). Regarding the central film thickness, in spite of its value being decreased with spin, the maximum film thickness in the contact area is observed to remain constant and its location to be shifted to the side with higher velocity. A complete analysis on this kind of contact was carried out by Dormois *et al.* in [15].

Case C corresponds to contacts with a fixed high spin value ($\Omega = 5000$ rad/s, B = 3.7) and variable degrees of starvation. Due to the presence of spin, a consistent asymmetry is shown in Figure 9. The effects of starvation are evidenced through a progressive loss of the overall film thickness in the contact. Moreover, contrary to case B, a more pronounced film thickness reduction is observed in $h_{m,+}$ than in its counterpart $h_{m,-}$ (60% against 15%); starvation thus reduces the influence of spin in the contact area. At the same time, the maximum film thickness value decreases at a higher rate than the minima (a total variation of 85% in this example), as also indicated in case A. The position of this value is observed to be in the same location as a result of the constant spin.

Case D, already underlined in Figure 8, corresponds to contacts with variable amounts of spin (from 0 to 5000 rad/s, in steps of 1000 rad/s), and a fixed quantity of lubricant upstream of its inlet of r_c = 1 (starved conditions). The behavior observed in this situation is similar to the one seen in case B. However, the set of curves in Figure 9 present now a general reduced film thickness because of the limitation in the available lubricant. Due to the spin, this reduction is not constant throughout the entire contact area. The maximum film thickness is independent of the spin value and is equal to the amount expected in a contact with no spin and the same quantity of lubricant at the contact inlet, as the corresponding starved situation in case A. This maximum is again shifted towards the side with higher velocity. Compared to case B, the film thickness variations in $h_{m,-}$ account to 25% against 10% for $h_{m,+}$.

Overall, under identical degree of starvation, introducing spin was observed to have little to no effect on the pressure profile, as revealed by Dowson *et al.* [9]. Significant changes in the pressure distribution were only confirmed by limiting the oil supply [53].

To further highlight the effect of starvation and spin on the entire contact area, four numerical interferograms have been selected from the set of results in Figure 8. The pictures in Figure 10 illustrate fully flooded and starved (r_c = 1) lubrication on the first and second row, and no spin and high spin ($B = 3.7$) conditions on the left and right column, respectively. The numerical interferograms reveal a similar aspect between the fully flooded and staved contacts and between the spinning and no spinning contacts. At the same time, the maximum film thickness is comparable between similarly lubricated contacts. For the 2 cases with spin in Figure 10, the velocity field is superimposed on the film thickness distribution. Under these conditions, the kinematic field is no longer unidirectional as it would be for the 2 no-spin cases on the left, but it varies in magnitude and direction under the effect of spin.

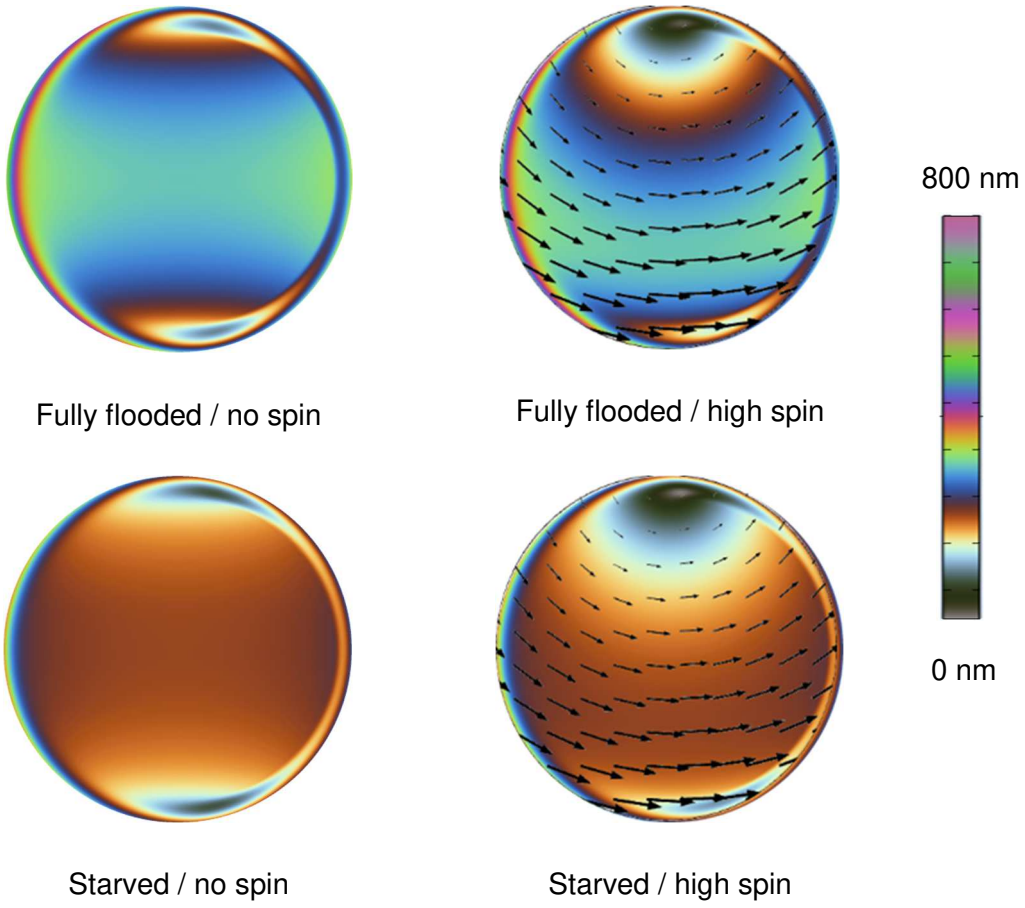

Figure 10. *Numerical interferograms for four selected cases presented in Figure 7, for fully flooded and starved (r_c = 1) conditions, without spin and with high spin (B = 3.7). The velocity distribution (in magnitude and direction) is superimposed on the film thickness field for the right-hand cases with high spin.*

Figure 11 reports the reduction rate of the critical minimum film thickness $h_{m,-}$ of a spinning contact as a function of its lubricant supply, for different spin values. The film thickness reduction rate is expressed as follows:

$$C_{st} = 1 - \left(h_{m,-}\right)_{st,sp} / \left(h_{m,-}\right)_{ff,sp} \quad (18)$$

with $\left(h_{m,-}\right)_{st,sp}$ the critical minimum film thickness under starvation (subscript st) and spinning (subscript sp) conditions and $\left(h_{m,-}\right)_{ff,sp}$ the film thickness of the same point under fully flooded (subscript ff) and identical spinning conditions. An arrow indicates the direction of the increasing degree of starvation and film thickness reduction. The points shown in blue concern the critical film thickness values, with spin, displayed in Figure 8 (L = 6.6 and M =272.3), whose operating conditions are summarized in Table 4. In addition, the reduction rate for three distinct contact conditions with no spin and variable oil supply are included. They are indicated in red (L = 6.2 and M =117.3), yellow (L = 7.4 and M =69.3) and green (L = 8.2 and M =51.1). Their operating conditions are those summarized in Table 1, with

entrainment speeds u_e of 0.16, 0.32 and 0.48 m/s, respectively. Experimental film thickness reduction factors C_{st} for these three conditions are equally shown in Figure 11. For those, the experimental setup employed was the one previously discussed in Section 3. Similar to Equation (16), the effect of starvation on the critical minimum film thickness has been quantified and fitted into an expression function of $h_{oil}/(h_c)_{ff,ns}$. The C_{st} reduction factor thus reads:

$$C_{st} = 1 - \frac{0.228}{\frac{h_{oil}}{(h_c)_{ff,ns}} + 0.223} \tag{19}$$

with h_{oil} the equivalent oil film thickness upstream of the contact inlet and $(h_c)_{ff,ns}$ the central film thickness under fully flooded conditions and no spinning.

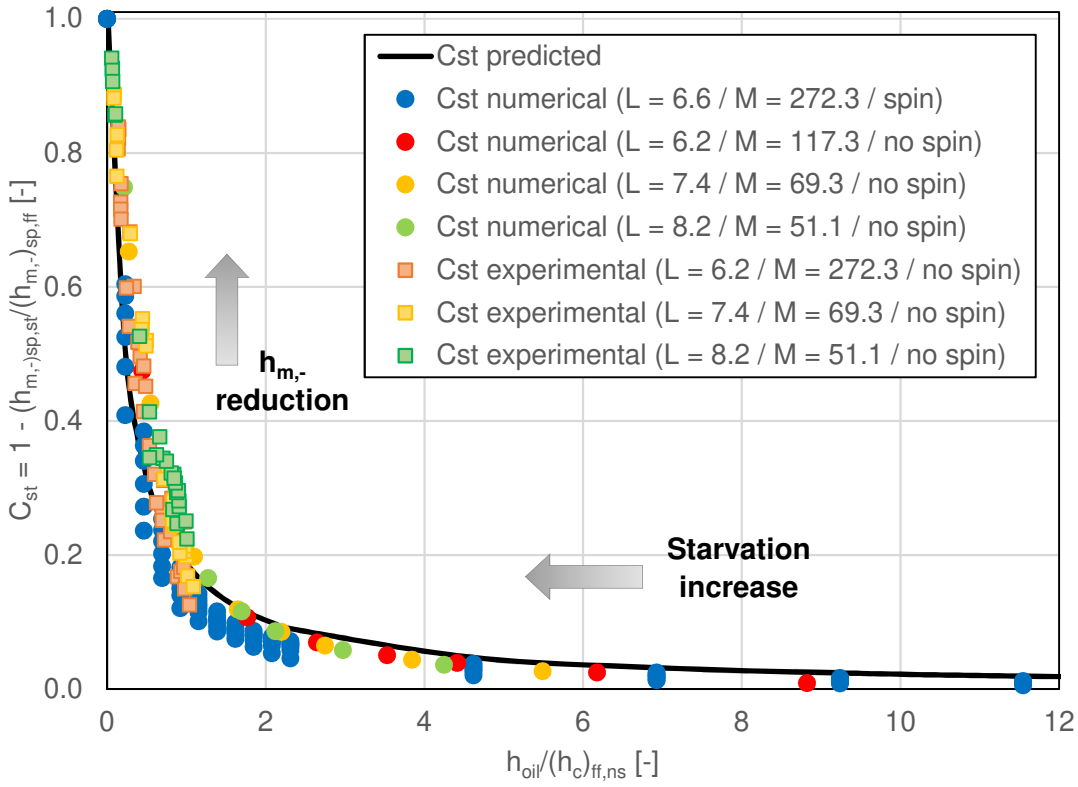

Figure 11. *Variation of the critical film thickness reduction C_{st} as a function of the oil supply and for different operating conditions (L and M pairs), with and without spinning. The arrows indicate the direction of increasing starvation and $h_{m,-}$ reduction.*

Equation (19) decouples the effect of starvation to that of associated to spinning. The graph in Figure 11 shows a reduction of the critical minimum film thickness with increasing degrees of starvation, regardless of the spinning condition chosen. The maximum deviation with respect to the predicted behavior corresponds to cases with high degrees of starvation. In these cases, the deviation with respect to the numerical value can reach up 10%. For mildly starved contacts (i.e. $h_{oil}/(h_c)_{ff,ns} > 1.5$), the deviation decreases to values below 5%.

The graph in Figure 8 shows that, under identical lubricant supply, an increase of the spin velocity entrains a reduction of the critical film thickness value (or increasing C_{st}). At the same time, by starving the contact, these differences are attenuated, limiting the film thickness reduction. This variation with the oil supply is, however, not linear. As can be observed in Figure 8, variations in the film thickness occur faster with higher degrees of starvation (steeper slope of the $R = h/h_{c,ff}$ relative the minimum film thickness).

To understand this behavior, two effects involving the velocity and pressure fields have to be considered. When no spin is in place, lubricant enters the contact at an equal speed along the y-direction. With spin, however, this is not the case. Indeed, the addition of a spin component to the velocity field generates a speed gradient within the contact area. Therefore, where faster local speeds are registered, more lubricant feeds the concerned contact region, whereas slower regions receive lower amounts. This entails that the effect of starvation on the local film thickness is more significant in the high velocity region $(Y < 0)$ than in its slower counterpart $(Y > 0)$. Thus, spin intensifies the local effects of starvation. As a result of this mechanism, starvation compensates the dissymmetry caused by spin. One can see this in Figure 8 (Case C) where the difference between both local minima is reduced with starvation. Secondly, spin has a limited effect on the pressure profile [54]. Starvation on the other hand inhibits the film formation capacity at the contact inlet and alters the pressure distribution to be more Hertzian-like in nature [23]. With a now smaller oil quantity entrapped within the contact region, the relative difference between the film thicknesses in both side lobes is also smaller. This can be observed when comparing the curves of Cases B and D in Figure 8. Although the original dissymmetry caused by the spin would still persist, the profiles tend to be more uniform. In fact, less oil is being redistributed from one side of the contact to the other by its internal flows, which are in turn entrained by spin.

Overall, the critical minimum film thickness value of a spinning and starved contact $(h_{m,-})_{st,sp}$ can be estimated following Equation (20), valid for the specific operating and lubrication conditions presented in this study. It follows a similar structure as the previous estimation for spinning and fully flooded contacts in Equation (17).

$$(h_{m,-})_{st,sp} = (h_{m,-})_{ff,ns} \cdot (1 - C_{sp}) \cdot (1 - C_{st}) \tag{20}$$

with C_{sp} the film thickness reduction factor due to spin, described in Equation (16), and C_{st} the film thickness reduction factor due to starvation, defined in Equation (19). $(h_{m,-})_{ff,ns}$ is the critical minimum film thickness under fully flooded conditions and no spin.

5. Conclusions

This paper presents a computational model able to evaluate the influence of starvation in large-size spinning isothermal contacts. The approach detailed herein serves as an extension to the model previously introduced for EHL modeling, and integrates both spinning kinematics and diphasic flows. The computational model has been validated experimentally

considering fully flooded and starved lubrication conditions and no spin. Transverse film thickness profiles are calculated for different spin and lubricant supply configurations. The focus is set on the critical minimum film thickness $h_{m,-}$. This work allows to draw the following conclusions:

(1) It has been found that the existence of a variable kinematic field, such as the one encountered in spinning contacts, affects the lubricant supply at the contact inlet region. Thus, the film thickness reduction in presence of spin differs from classical starvation and becomes irregular along the transversal direction of the flow. However, it was also seen that spin had little to no effect on the maximum film thickness in the contact area, even in the presence of starvation.

(2) The effects of starvation adds to those of spinning. While it has been seen that spinning generates local maxima and minima at opposite sides of the contact area, starvation further reduces the overall film thickness. When exposed to both phenomena, the film thickness reduction is more important in the local maxima region, where the local speed is faster, than in the local minima. The same variations in the kinematic field that induce dissymmetry in the film thickness profile also attenuates these differences.

(3) The effect of both spin and starvation, in terms of film thickness change can be successfully quantified. This has been done by comparing the critical film thickness under specific operating and lubrication conditions to a reference film thickness.

Acknowledgements

This work was supported as part of the “Advanced Bearing Lubrication” program established between INSA Lyon, INSAVALOR and the SKF Company, which is gratefully acknowledged. The authors also thank Nicolas Devaux and Lionel Lafarge for their support in the experimental work.

Nomenclature

Variable	Unit	Description
a	[m]	Hertzian contact radius
A_1, A_2, b_1, b_2, C_1, C_2	[varying]	Constants of the modified WLF model
B	[-]	Modified spin-to-roll ratio ($B = 2\Omega a/u_e$)
C_{sp}	[-]	Film reduction coefficient due to spinning
C_{st}	[-]	Film reduction coefficient due to starvation
c_l	[m·s^{-1}]	Velocity of sound at bubble point pressure
c_v	[m·s^{-1}]	Velocity of sound at wet point pressure
E	[Pa]	Young modulus
E'	[Pa]	Equivalent Young modulus
F	[-]	Pressure term in modified WLF equation
G	[-]	Dimensionless material parameter ($G = \alpha^* E'$)
h	[m]	Gap film thickness
h_0	[m]	Rigid body displacement at the contact center
h_c	[m]	Film thickness at the geometrical center of the contact
h_f	[m]	Fluid film thickness
$h_{m,-}$	[m]	Critical minimum film thickness ($Y > 0$)
$h_{m,+}$	[m]	Local minimum film thickness at $Y < 0$
h_{max}	[m]	Maximum film thickness in the contact area
h_{oil}	[m]	Film thickness of the oil layer supplied at the contact inlet
K_0	[-]	Bulk modulus at environment conditions
K_0'	[-]	Pressure-dependency rate of the bulk modulus
K_{00}	[-]	Bulk modulus at T = 0 K
L	[-]	Dimensionless load parameter (Moes) ($L = G(2U)^{0.25}$)
M	[-]	Dimensionless material parameter (Moes) ($M = W(2U)^{-0.75}$)
R	[-]	Film thickness reduction ($R = h/h_{c,ff}$)
r_c	[-]	Relative oil film thickness ($r_c = h_{oil}/(\bar{\rho}_c h_{c,ff})$
R_x	[m]	Curvature radius along the x-axis
R_y	[m]	Curvature radius along the y-axis
S_P	[m^2]	Hertzian contact area
T	[°C]	Temperature
T_0	[°C]	Environment temperature
T_g	[°C]	Glass transition temperature at a given pressure
$T_{g,0}$	[°C]	Glass transition temperature at ambient pressure
p	[Pa]	Pressure
p_H	[Pa]	Hertzian pressure
P_{sat}	[Pa]	Bubble point pressure
P_{vm}	[Pa]	Wet point pressure
U	[-]	Dimensionless velocity ($U = \mu_0 u_e/(E' R_x)$)
$u_{e,j,0}$	[m·s^{-1}]	Entrainment velocity in the j-direction at the contact center
$u_{i,j}$	[m·s^{-1}]	Velocity of solid i in the j-direction
$u_{i,j,0}$	[m·s^{-1}]	Velocity of solid i in the j-direction at the contact center
w	[N]	Load
W	[-]	Dimensionless load ($W = w/(E' R_x^2)$)
x	[m]	Coordinate in the direction of flow
y	[m]	Coordinate perpendicular to the direction of flow
Y	[-]	Dimensionless coordinate perpendicular to the direction of flow ($Y = y/a$)
α^*	[Pa^{-1}]	Pressure-viscosity coefficient
β_k	[K^{-1}]	Bulk modulus-temperature coefficient
δ	[-]	Elastic deformation of the solids in contact

μ	[Pa·s]	Viscosity
μ_0	[Pa·s]	Viscosity at room conditions
μ_g	[Pa·s]	Viscosity at the glass transition temperature
ν	[-]	Poisson ration
θ	[-]	Fraction film content
ρ	[kg·m^{-3}]	Density
ρ_0	[kg·m^{-3}]	Density at room conditions
ρ_c	[kg·m^{-3}]	Density at the geometrical center of the contact
ρ_f	[kg·m^{-3}]	Density of the fluid lubricant
ρ_l	[kg·m^{-3}]	Density at bubble point pressure

Subscript	**Description**
ff	Fully flooded lubrication conditions
st	Starved lubrication conditions
sp	Spinning
ns	No spinning

References

[1] B. Hamrock and D. Dowson, "Isothermal elastohydrodynamic lubrication of point contacts - Part I: Theoretical formulation," ASME J Tribol, vol. 98, no. 2, pp. 223-228, 1976.

[2] B. Hamrock and D. Dowson, "Isothermal elastohydrodynamic lubrication of point contacts - Part II: Ellipticity parameter results," ASME J Tribol, vol. 98, no. 3, pp. 375-383, 1976.

[3] R. Chittenden, D. Dowson, J. Dunn and C. Taylor, "A Theoretical Analysis of the Isothermal Elastohydrodynamic Lubrication of Concentrated Contacts - Part 1: Direction of Lubricant Entrainment Coincident with the Major Axis of the Hertzian Contact Ellipse," Proc R Soc London, vol. A397, pp. 245-269, 1985.

[4] R. Chittenden, D. Dowson, J. Dunn and C. Taylor, "A Theoretical Analysis of the Isothermal Elastohydrodynamic Lubrication of Concentrated Contacts - Part 2: General Case, with Lubricant Entrainment along Either Principal Axis of the Hertzian Contact Ellipse or at Some Intermediate Angle," Proc R Soc London, vol. A397, pp. 271-294, 1985.

[5] C. Venner and A. Lubrecht, "Revisiting film thickness in slender elasto-hydrodynamically lubricated contacts," Proc IMechE, Part C: J Mech Eng Sci, vol. 224, no. 12, pp. 2549-58, 2010.

[6] R. Snidle and J. Archard, "Theory of hydrodynamic lubrication for a spinning sphere," Proc Inst Mech Eng, vol. 184, no. 1, pp. 839-848, 1969.

[7] S. Poon, "Some calculations to assess the effect on the tractive capacity of rolling contact drives," Proc Inst Mech Eng, vol. 185, no. 1, pp. 1015-1022, 1970.

[8] D. Dowson, C. Taylor and H. Xu, "The lubrication of elliptical contacts with spin," Proceedings of the 13th Leeds-Lyon Symposium on Tribology "Fluid Film Lubrication - Osborne Reynolds Centenary", Leeds 8-12 September 1986, Tribology Series, vol. 11, pp. 451-463, 1987.

[9] D. Dowson, C. M. Taylor and H. Xu, "Elastohydrodynamic lubrication of elliptical contacts with spin and rolling," Proc IMechE, Part C: J Mech Eng Sci, vol. 205, pp. 165-174, 1991.

[10] D. Dowson, C. M. Taylor and H. Xu, "Elastohydrodynamic lubrication of elliptical contacts with pure spin," Proc IMechE, Part C: J Mech Eng Sci, vol. 207, pp. 83-92, 1993.

[11] P. Yang and J. Cui, "The influence of spinning on the performance of EHL in elliptical contacts," Proceedings of the IUTAM Symposium on Elastohydrodynamics and Micro-elastohydrodynamics, Cardiff 1-3 September 2004, Springer, pp. 81-92, 2006.

[12] Q. Zou, C. Huang and S. Wen, "Elastohydrodynamic film thickness in elliptical contacts with spinning and rolling," ASME J Tribol, vol. 121, pp. 686-692, 1999.

[13] F. Colin, F. Chevalier, J.-P. Chaomleffel, J. de Mul and G. Dalmaz, "Starved elastohydrodynamic lubrication of the rib-roller end contact in tapered roller bearings:

film thickness, traction and moments," Proceedings of the 24th Leeds-Lyon Symposium on Tribology "Tribology for Energy Conservation", London 4-6 September 1997, Tribology Series, vol. 34, Elsevier, pp. 253-263, 1998.

[14] M. Taniguchi, D. Dowson and C. M. Taylor, "The effect of spin motion upon elastohydrodynamic elliptical contacts," Proceedinfgs of the 23rd Leeds-Lyon Symposium on Tribology " Elastohydrodynamics - '96 Fundamentals and Applications in Lubrication and Traction", Leeds 10-13 September 1996, Tribology Series, vol. 32, Elsevier, pp. 599-610, 1997.

[15] H. Dormois, N. Fillot, W. Habchi, G. Dalmaz, P. Vergne, G. Morales-Espejel and E. Ionnades, "A numerical study of friction in isothermal EHD rolling-sliding sphere-plane contacts with spinning," ASME J Tribol, vol. 132, no. 2, pp. 021501-10, 2010.

[16] T. Doki-Thonon, N. Fillot, P. Vergne and G. Morales-Espejel, "Numerical insight into heat transfer and power losses in spinning EHL non-Newtonian point contacts," Proc IMechE, Part J: J Eng Tribol, vol. 226, no. 1, pp. 23-35, 2012.

[17] T. Doki-Thonon, N. Fillot, G. E. Morales-Espejel, D. Philippon, N. Devaux and P. Vergne, "A dual experimental / numerical approach for film thickness analysis in TEHL spinning skewing circular contacts," Tribol Lett, vol. 50, no. 1, pp. 115-126, 2013.

[18] J.-D. Wheeler, N. Fillot, D. Philippon, N. Devaux, G. E. Morales-Espejel and P. Vergne, "A numerical and experimental approach of the flange-roller end contact," Proc of the International Tribology Conference ITC2015, Tokyo, 16-20 September, Japanese Society of Tribologists, 2015.

[19] J.-D. Wheeler, N. Fillot, P. Vergne, D. Philippon and G. E. Morales-Espejel, "On the crucial role of ellipticity on elastohydrodynamic film thickness and friction," Proc IMechE, Part J: J Eng Tribol, vol. 230, no. 12, pp. 1503-1515, 2016.

[20] W. Habchi, I. Demirci, D. Eyheramendy, G. E. Morales-Espejel and P. Vergne, "A finite element approach of thin film lubrication in circular EHD contacts," Tribol Inter, vol. 40, no. 10-12, pp. 1466-1473, 2007.

[21] H. Dormois, N. Fillot, P. Vergne, G. Dalmaz, M. Querry and E. Ioannides, "First traction results of high spinning large-size circular EHD contacts from a new test rig: Tribogyr," Tribol Trans, vol. 52, no. 2, pp. 171-179, 2009.

[22] N. Gadallah and G. Dalmaz, "Hydrodynamic lubrication of the rib-roller end contact of a tapered roller bearing," ASME J. Tribol, vol. 106, no. 2, pp. 265-272, 1984.

[23] L. D. Wedeven, D. Evans and A. Cameron, "Optical analysis of ball bearing starvation," ASME J Lubr Tech, vol. 93, no. 3, pp. 349-361, 1971.

[24] F. Chevalier, A. Lubrecht, P. Cann, F. Colin and G. Dalmaz, "Film thickness in starved EHL point contacts," ASME J Tribol, vol. 120, no. 1, pp. 126-133, 1998.

[25] B. Damiens, C. Venner, P. Cann and A. Lubrecht, "Starved lubrication of elliptical EHD contacts," ASME J Tribol, vol. 126, no. 1, pp. 105-111, 2004.

[26] P. Svoboda, D. Kostal, I. Krupka and M. Hartl, "Experimental study of starved EHL contacts based on thickness of oil layer in the contact inlet," Tribol Inter, vol. 67, pp. 140-

145, 2013.

[27] W. Habchi, D. Eyheramendy, P. Vergne and G. E. Morales-Espejel, "A full-system approach to the elastohydrodynamic line/point contact problem," ASME J Tribol, vol. 130, no. 1, pp. 21501-10, 2008.

[28] W. Habchi, D. Eyheramendy, S. Bair, P. Vergne and G. Morales-Espejel, "Thermal elastohydrodynamic lubrication of point contacts using a Newtonian/generalized Newtonianl lubricant," Tribol Lett, vol. 30, no. 1, pp. 41-52, 2008.

[29] T. Doki-Thonon, "Thermal effects in elastohydrodynamic spinning circular," PhD thesis (in English), Institut National des Sciences Appliquées de Lyon, Villeurbanne (France), 2012, no. 2012ISAL0058, http://theses.INSA-lyon.fr/publication/2012ISAL0058/these.pdf

[30] S. Bair, C. Mary, N. Bouscharain and P. Vergne, "An improved Yasutomi correlation for vscosity at high pressure," Proc IMechE, Part J: J Eng Tribol, vol. 227, no. 9, pp. 1056-1060, 2013.

[31] H. G. Elrod and M. Adams, "A computer program for cavitation and starvation problems," Proc of the 1st Leeds-Lyon Symposium on Tribology "Cavitation and Related Phenomena in Lubrication", Leeds September 1974, Mechanical Engineering Publication, pp. 37-41, 1975.

[32] H. Elrod, "A cavitation algorithm," ASME J Lubr Tech, vol. 103, no. 3, pp. 350-354, 1981.

[33] G. Bayada, M. Chambat and M. El Alaoui, "Variational formulations and finite element algorithms for cavitation problems," ASME J Tribol, vol. 112, no. 2, pp. 398-403, 1990.

[34] G. Bayada, M. Chambat and C. Vázquez, "Characteristics method for the formulation and computation of a free boundary cavitation problem," J Computational and Applied Mathematics, vol. 98, no. 2, pp. 191-212, 1998.

[35] C. Gu, X. Meng and Y. Xie, "A universal model for both flooded and starved lubrication regimes and its application in ring-liner system," Tribol Trans, vol. 60, no. 3, pp. 506-515, 2017.

[36] H. Swift, "The stability of lubricating films in journal bearings," Minutes of the Proceedings of the Institution of Civil Engineers, vol. 233, no. 232, pp. 267-288, 1932.

[37] W. Stieber, Das Schwimmlager: Hydrodynamische Theorie, Berlin (Germany): VDI Verlag, 1933.

[38] S. Wu, "A penalty formulation and numerical approximation of the Reynolds-Hertz problem of elastohydrodynamic lubrication," Inter J Eng Science, vol. 24, no. 6, pp. 1001-1013, 1986.

[39] D. Dowson and C. Taylor, "Fundamental aspects of cavitation in bearings," Proc of the 1st Leeds-Lyon Symposium on Tribology "Cavitation and Related Phenomena in Lubrication", Leeds September 1974, Mechanical Engineering Publication, pp. 15-25, 1975.

[40] M. Braun and R. Hendricks, "An experimental investigation of the vaporous/gaseous cavity characteristics of an eccentric journal bearing," ASLE Trans, vol. 27, no. 1, pp. 1-

14, 1984.

[41] I. Etsion and L. Ludwig, "Observation of pressure variationin the cavitation region of submerged journal bearings," J Lubr Tech, vol. 104, no. 2, pp. 157-163, 1982.

[42] D. Vijayaraghvan and T. G. Keith, "An efficient, robust, and time accurate numerical scheme applied to a cavitation algorithm," ASME J Tribol, vol. 112, no. 1, pp. 44-51, 1990.

[43] M. Fensanghary and M. Khonsari, "A modification of the switch function in the Elrod cavitation algorithm," ASME J Tribol, vol. 133, no. 2, p. 024501, 2011.

[44] F. Sahlin, A. Almqvist, L. Larsson and S. Glavatskih, "A cavitation algorithm for arbitrary lubricant compressibility," Tribol Inter, vol. 40, pp. 1294-1300, 2007.

[45] D. van Odyck and C. Venner, "Compressible Stokes flow in thin films," ASME J Tribol, vol. 125, pp. 543-551, 2003.

[46] G. Bayada and L. Chupin, "Compressible fluid model for hydrodynamic lubrication cavitation," ASME J Tribol, vol. 135, no. 4, pp. 041702-15, 2013.

[47] G. Bayada, "From a compressible fluid model to new mass conserving cavitation algorithms," Tribol Inter, vol. 71, pp. 38-49, 2014.

[48] J. Molimard and M. V. P. Querry, "Lubricant rheology in real conditions: measurements and confrontation with a ball/disk contact," Revue de Métallurgie, vol. 98, no. 2, pp. 141-148, 2002.

[49] P. Cusseau, P. Vergne, L. Martinie, D. Philippon, N. Devaux and F. Briand, "Film forming capability of polymer-base oil lubricants in elastohydrodynamic and very thin film regimes," Tribol Lett, vol. 67, no. 2, p. 45, 2019.

[50] J. Molimard, M. Querry and P. Vergne, "New tools for the experimental study of EHD and limit lubrication," 25th Leeds-Lyon Symposium on Tribology “Lubrication at the Frontier”, Lyon 8-11 September 1998, Tribology Series, vol. 36, Elsevier, pp. 717-726, 1999.

[51] J.-D. Wheeler, J. Molimard, N. Devaux, D. Philippon, D. Fillot, P. Vergne and G. Morales-Espejel, "A generalized differential colorimetric interferometry method: extension to the film thickness measurement of any point contact geometry," Tribol Trans, vol. 61, no. 4, pp. 648-660, 2018.

[52] H. Moes, "Optimum similarity analysis with applications to elastohydrodynamic lubrication," Wear, vol. 159, no. 1, pp. 57-66, 1992.

[53] L. D. Wedeven, D. Evans and A. Cameron, "Optical analysis of ball bearing starvation," NASA TM X-52869, 1970.

[54] D. Dowson, C. Taylor and H. Xu, "Elastohydrodynamic lubrication of elliptical contacts with spin and rolling," Proc IMechE, Part C: J Mech Eng Sci, vol. 205, pp. 165-174, 1991.

Annex

The following Tables list the coefficients for the modified Yasutomi-WLF correlation and the Murnaghan EOS for the two lubricants employed in this study.

Parameter [unit]	Lubricant 1	Lubricant 2
A_1 [°C]	61.00	188.86
A_2 [Pa^{-1}]	$1.04 \cdot 10^{-9}$	$0.72 \cdot 10^{-9}$
b_1 [Pa^{-1}]	$5.97 \cdot 10^{-9}$	$8.20 \cdot 10^{-9}$
b_2 [-]	-0.60	-0.53
C_1 [-]	16.00	16.09
C_2 [°C]	29.80	17.38
$T_{g,0}$ [°C]	-83.40	-83.21
μ_G [Pa·s]	$1 \cdot 10^{12}$	$1 \cdot 10^{12}$

Table 5. *Parameters of the modified Yasutomi-WLF correlation for lubricants 1 and 2.*

Parameter [unit]	Lubricant 1	Lubricant 2
a_v [K^{-1}]	$8.88 \cdot 10^{-4}$	$7.33 \cdot 10^{-4}$
β_k [K^{-1}]	$6.60 \cdot 10^{-3}$	$6.09 \cdot 10^{-3}$
K_{00} [Pa]	$1.08 \cdot 10^{10}$	$9.23 \cdot 10^{9}$
K_0' [-]	10.22	10.55
T_R [K]	298	298
ρ_R [kg/m^3]	973	872

Table 6. *Parameters of the Murnaghan EOS for lubricants 1 and 2.*

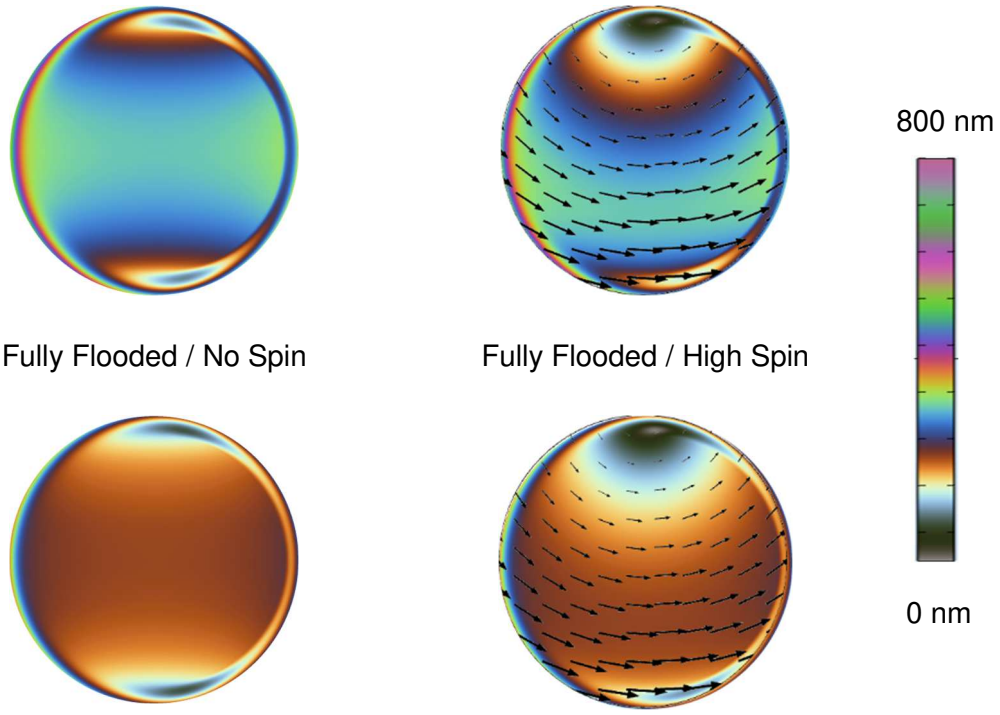

Fully Flooded / No Spin

Fully Flooded / High Spin

Starved / No Spin

Starved / High Spin

Numerical interferograms of 4 cases combining spin and no spin, as well as fully-flooded and starved conditions.